The Cryosphere Discuss., 8, 4195–4241, 2014
www.the-cryosphere-discuss.net/8/4195/2014/
doi:10.5194/tcd-8-4195-2014

The Cryosphere Discussions
Open Access

Cloud and precipitation properties from ground-based remote sensing instruments in East Antarctica

I. V. Gorodetskaya[1], S. Kneifel[2,3], M. Maahn[2], K. Van Tricht[1], J. H. Schween[2], S. Crewell[2], and N. P. M. Van Lipzig[1]

[1]Department of Earth & Environmental Sciences, KU Leuven – University of Leuven, Heverlee, Belgium
[2]Institute for Geophysics and Meteorology, University of Cologne, Cologne, Germany
[3]McGill University, Montreal, Canada

Received: 6 June 2014 – Accepted: 16 June 2014 – Published: 28 July 2014

Correspondence to: I. V. Gorodetskaya (irina.gorodetskaya@ees.kuleuven.be)

Published by Copernicus Publications on behalf of the European Geosciences Union.

Abstract

A new comprehensive cloud-precipitation-meteorological observatory has been established at Princess Elisabeth base, located in the escarpment zone of Dronning Maud Land, East Antarctica. The observatory consists of a set of ground-based remote sensing instruments (ceilometer, infrared pyrometer and vertically profiling precipitation radar) combined with automatic weather station measurements of near-surface meteorology, radiative fluxes, and snow accumulation. In this paper, the observatory is presented and the potential for studying the evolution of clouds and precipitating systems is illustrated by case studies. It is shown that the synergetic use of the set of instruments allows for distinguishing ice, mixed-phase and precipitating clouds, including some information on their vertical extent. In addition, wind-driven blowing snow events can be distinguished from deeper precipitating systems. Cloud properties largely affect the surface radiative fluxes, with liquid-containing clouds dominating the radiative impact. A statistical analysis of all measurements (in total 14 months mainly occurring in summer/autumn) indicates that these liquid-containing clouds occur during as much as 20 % of the cloudy periods. The cloud occurrence shows a strong bimodal distribution with clear sky conditions 51 % of the time and complete overcast conditions 35 % of the time. Snowfall occurred 17 % of the cloudy periods with a predominance of light precipitation and only rare events with snowfall $> 1\,\mathrm{mm\,h^{-1}}$ water equivalent (w.e.). Three of such intensive snowfall events occurred during 2011 contributing to anomalously large annual snow accumulation. This is the first deployment of a precipitation radar in Antarctica allowing to assess the contribution of the snowfall to the local surface mass balance. It is shown that on the one hand large accumulation events ($> 10\,\mathrm{mm\,w.e.\,day^{-1}}$) during the measurement period of 26 months were always associated with snowfall, but that on the other hand snowfall did not always lead to accumulation. In general, this promising set of robust instrumentation allows for improved insight in cloud and precipitation processes in Antarctica and can be easily deployed at other Antarctic stations.

TCD
8, 4195–4241, 2014

1 Introduction

Knowledge of the Antarctic hydrologic cycle is essential in order to assess potential future changes of the Antarctic surface mass budget (SMB), which is one of the factors affecting global sea level (IPCC, 2013; Gregory and Huybrechts, 2006; Krinner et al., 2007; Ligtenberg et al., 2013; Rignot et al., 2011; Uotila et al., 2007; Van den Broeke et al., 2011). Clouds are among key components of the hydrologic cycle serving as the agents linking water vapor transport into Antarctica with precipitation, determining its amount and spatial distribution. Correct representation of cloud condensate amount and phase partitioning in climate models is crucial for simulation of Antarctic precipitation timing and spatial distribution, especially when orographic effects are present (Wacker et al., 2009). Via their radiative forcing, clouds also play a significant role in the Antarctic surface energy budget affecting air and surface temperatures and heat flux exchange of the snow surface with the air above and deeper snow layers (Bintanja and Van den Broeke, 1996; Van den Broeke et al., 2006; Vihma et al., 2011). Bennartz et al. (2013) demonstrated a dramatic example of cloud influence on the ice sheet surface energy budget, where radiative forcing of mixed-phase clouds coupled with warm air advection was responsible for the surface melt on top of the Greenland ice sheet in July 2012. Liston et al. (1999) pointed out that cloud radiative forcing is a potential player in sub-surface melt water production in the Antarctic near-coastal blue-ice areas.

The extreme environment and climate of the Antarctic ice sheet both lead to unique cloud properties and poses significant difficulties in cloud and precipitation observations. Low temperatures favor formation of thin ice clouds at all heights including near the surface during the entire year as compared to their occurrence globally only in the upper troposphere (Grenier et al., 2009; Bromwich et al., 2012). Thin ice clouds can have an important effect on the surface and top-of-atmosphere energy budget in the polar regions (Girard and Blanchet, 2001; Lampert et al., 2009). Further, mixed-phase clouds containing supercooled liquid water at air temperatures as low as −38 °C to −40 °C (below which homogeneous ice nucleation occurs) have been observed over

TCD
8, 4195–4241, 2014

the Antarctic ice sheet during short measurement campaigns (Lachlan-Cope, 2010; Walden et al., 2005). Presence of liquid has an important effect on cloud radiative properties by increasing cloud optical thickness and longwave emissivity (e.g., Turner et al., 2007). It is also an important player in precipitation formation favoring ice particle growth (Hogan et al., 2003a; Morrison and Pinto, 2005; Shupe and Intrieri, 2004; Sun and Shine, 1994). Identifying ice and mixed phase clouds is thus of high importance for understanding both precipitation processes and energy budget over the Antarctic ice sheet.

Another important challenge in the polar climate science is to understand complex mechanisms controlling snow accumulation at different time and spatial scales (Frezzotti et al., 2007, 2013). In particular, this refers to attributing the local and regional accumulation variability to the snowfall and/or drifting/blowing snow. Local snow accumulation is not necessarily driven by precipitation and at the same time precipitation-driven accumulation can be greatly reduced due to the drifting snow erosion (Das et al., 2013; Groot Zwaaftink et al., 2013; Lenaerts et al., 2012a, b). Drifting snow sublimation also may have a significant contribution to the snow ablation especially in the high katabatic wind regions (Lenaerts et al., 2012a, b; Thiery et al., 2012).

A new comprehensive observatory on cloud-precipitation-meteorological interactions has been established in the escarpment zone of Dronning Maud Land, East Antarctica, aiming to improve understanding of Antarctic cloud properties and different components of the SMB. The observatory consists of a set of basic and robust ground-based remote sensing instruments, namely, ceilometer, infrared pyrometer and vertically profiling precipitation radar (the only precipitation radar over the Antarctic ice sheet until now). In addition, an automatic weather station (AWS) provides hourly mean near-surface meteorology, surface radiative fluxes, 1 m snow temperature profile and snow accumulation (Gorodetskaya et al., 2013).

This specific combination of ground-based remote sensing measurements is intended to derive several key cloud and precipitation characteristics, including vertical structure of clouds and precipitation, cloud base height and temperature, identification

TCD
8, 4195–4241, 2014

of ice-only and mixed-phase clouds, and precipitation intensity. Further, the occurrence of ice virga (precipitation not reaching the surface) and its association with liquid cloud layers can be studied. Combination of the ground-based remote sensing instruments with an AWS allows studying cloud radiative forcing and relating snow accumulation to precipitation with a potential to distinguish between local accumulation due to snowfall or clear sky drifting snow. The goal of collecting these data is to perform detailed process-based model evaluation and improve cloud and precipitation parameterizations, required for the Antarctic climate simulations (Bromwich et al., 2012; Gallée and Gorodetskaya, 2010; Wacker et al., 2009). Furthermore, the data can be used to evaluate and complement satellite data from similar sensors.

The present paper demonstrates the potential of the observatory by providing detailed case studies and presents statistics of cloud and precipitation properties based on the available measurement periods during 2010–2013. In addition, year-around radar snowfall measurements during 2012 are used for snowfall analysis together with snow accumulation. It gives insight about the ice and mixed-phase cloud properties, precipitation intensity and height, contribution of snowfall to SMB, and occurrence of strong blowing snow events. The paper is structured as following: historical background related to cloud and precipitation measurements is given in Sect. 2, the observatory and data post-processing are described in Sect. 3, results are provided in Sect. 4 subdivided into two parts – case studies and a statistical analysis based on the available measurement periods. Conclusions are given in Sect. 5.

2 Historical background

Observations of clouds and precipitation in Antarctica can be dated back to the first exploratory expeditions, most notably year-around hourly meteorological observations during de Gerlache expedition on board Belgica during 1898–1899 and Roald Amundsen's expedition to the South Pole in 1911–1912. During both expeditions, detailed information on cloud amounts, types and snowfall was recorded (Arctowski, 1904;

TCD
8, 4195–4241, 2014

Mohn, 1915). The longest cloud and precipitation records in Antarctica (since 1950s) are available via visual observations of cloudiness, cloud types, precipitation and other weather phenomena at several year-around Antarctic stations (Averianov, 1990; Bryazgin, 1990; Hahn and Warren, 2003; Turner and Pendlebury, 2004; Rusin, 1964). Since the beginning of satellite era in 1979, cloud occurrence and some properties have been derived from passive satellite observations, however serious limitations were encountered over ice/snow surfaces (Berque et al., 2011; Lazzara et al., 2003; Town et al., 2007). Launch of active sensors (lidar and radar) on the A-train satellites (Stephens et al., 2002) marks another important step especially for polar cloud observation providing vertical profiles of cloud and precipitation microphysical and radiative properties (e.g., Grenier et al., 2009; Winker et al., 2010; Henderson et al., 2013). Cloud fraction and optical thickness have also been approximated using near-surface broadband longwave radiation measurements (Kuipers Munneke et al., 2011; Town et al., 2007; Van den Broeke et al., 2006). Recently available advanced ground-based remote sensing and airborne in-cloud measurement techniques provide valuable insights into cloud microphysical properties (e.g., Del Guasta et al., 1993; Lachlan-Cope, 2010; Morley et al., 1989), however are usually limited to short periods requiring significant maintenance efforts, costs, and power/logistics demands. Bromwich et al. (2012) provides an extensive overview of existing Antarctic cloud data from various measurement techniques.

3 HYDRANT observatory

3.1 Overview

The Antarctic environment with its especially harsh conditions and difficult accessibility calls for measurements using robust instruments requiring minimal maintenance, but which still provide crucial information on cloud and precipitation properties on a long term. The HYDRANT project ("The atmospheric branch of the hydrologic cycle

TCD
8, 4195–4241, 2014

in Antarctica") tries to fulfill this demand with its set of ground based remote sensing instruments providing high vertical and temporal resolution of cloud and precipitation properties on a long-term combined with near-surface meteorological and snow accumulation measurements. The base for our measurements is the Princess Elisabeth (PE) station built on the Utsteinen Ridge, north of the Sør Rondane mountain chain, in Dronning Maud Land (DML), in the escarpment zone of the East Antarctic plateau (71°57' S, 23°21' E, 1392 m a.m.s.l., 173 km from the coast (Fig. 1), (see also Pattyn et al., 2009). Inaugurated in February 2009, PE base is designed as zero-emission station relying mostly on wind and solar power (http://www.antarcticstation.org/). Manned only during summer season (November–February), the station itself and the research instruments are controlled remotely via satellite connection year around. Such a concept minimizes local emissions, which can be particularly important not only for boundary-layer aerosol measurements, but also for cloud properties downwind due to the role of aerosols in cloud formation and the relatively pristine Antarctic atmosphere.

The measurement site is characterized by relatively mild climate with a rather high frequency of synoptic events under cyclonic influence and a lack of katabatic drainage of cold air from the plateau due to mountain sheltering (Gorodetskaya et al., 2013). Strong easterly winds are associated with synoptic regimes, while south-southeasterly relatively weak winds are mostly of katabatic origins. The low katabatic wind speeds together with cloud-free skies lead to significant surface cooling and building up of strong temperature inversions (Gorodetskaya et al., 2013; Thiery et al., 2012).

An overall description of the HYDRANT instruments and their measurement periods are given in Table 1. Detailed description of the cloud and precipitation ground-based remote sensing instruments and their products are given in Tables 2–4. The instruments include (i) – a ceilometer (Table 2), providing vertical profiles of atmospheric attenuated backscatter coefficients from which one can derive cloud base height, cloud vertical structure and information on cloud phase; (ii) – an infra-red pyrometer (Table 3) providing effective cloud base temperature; (iii) – a Micro Rain Radar (MRR) (Table 4) providing vertical profiles of spectral signal power, from which one can derive effec-

TCD
8, 4195–4241, 2014

tive radar reflectivity factor Z_e (hereafter referred as radar reflectivity), mean Doppler velocity of the falling particles, and spectral width. The MRR was originally designed to derive properties of rain (drop size distribution, rain rate) using a relation between drop sizes and fall speed. Recently, new algorithms have been developed extending MRR application to solid precipitation (Colle et al., 2014; Kneifel et al., 2011; Maahn and Kollias, 2012). In addition, a webcam is installed on the PE roof facing the ground-based instruments and Utsteinen nunatak, providing weather, cloud and instrument monitoring.

Cloud and precipitation measurements are combined with AWS measurements providing hourly data on the near-surface air temperature, relative humidity with respect to ice (RH_i), wind speed and direction, pressure, incoming and outgoing longwave (LW) and shortwave (SW) radiative fluxes, 1 m snow temperature profile and net snow height changes. Yearly snow density measurements are performed every summer season in the AWS vicinity to convert measured snow accumulation during the previous year to water equivalent (w.e.) (see Gorodetskaya et al., 2013, for details).

The project website (http://ees.kuleuven.be/hydrant) contains raw data quicklooks, information about the instruments and measurement campaigns, as well as information about available data products. Data are stored as netCDF files and are freely available upon request via the project website.

3.2 Remote sensing data and post-processing methods

All remote sensing instruments are installed next to each other on the PE base roof pointing vertically (Fig. 1). Such installation avoids obstacles in the field of view and ensures that different instruments observe as close as possible volume (see Tables 2–4 for the instruments fields of view). Location on the roof of the base about 10 m above the snow surface also minimizes the insrument view obscurance by shallow drifting snow.

TCD
8, 4195–4241, 2014

3.2.1 Ceilometer: cloud height and phase

The ceilometer, manufactured by Vaisala (Finland), is a single wavelength lidar system without polarization with emitted laser pulse wavelength of 910 nm (Table 2). It reports attenuated backscatter profile ($\beta_a = \beta(z)\tau^2(z)$, $sr^{-1}\,m^{-1}$), derived using the lidar equation by the Vaisala processing system (Münkel et al., 2006; Pal et al., 1992). Here $\beta(z)$ is the true backscatter coefficient at distance z for the wavelength of the emitted laser pulse, and $\tau^2(z)$ is the two-way attenuation of the lidar signal due to the transmittance of the atmosphere between the lidar and the scattering volume. Useful reported β_a profile ranges from 10 m up to 7700 m above ground level (a.g.l.) with 10 m vertical resolution. The reported β_a includes range normalization by multiplying the received ceilometer power with z^2. It also includes sensitivity normalization by calibrating the signal with the instrument-specific factors (Münkel et al., 2006). Percentage of the window transmission is continuously reported and except for strong snowfall events it has been > 99 % maintained by window ventilation and heating. The final Vaisala raw measurement profile of β_a (at 15 s temporal resolution) contains noise reduction by summing multiple high-frequency backscatter pulses.

Cloud/precipitation occurrence and base height are identified using the Polar Threshold (PT) algorithm developed specifically for polar regions (Van Tricht et al., 2014). The algorithm identifies the lowest boundary of a hydrometeor layer including optically thin clouds and precipitation ice layers, frequently observed at low levels. Although the ceilometer does not have polarization capability, which would provide direct information on the cloud phase, the high backscatter coefficient of the liquid-containing layers together with the rapid extinction of the lidar signal makes it possible to distinguish the liquid-containing clouds as geometrically thin but highly reflective layers (Hogan et al., 2003b). Hogan et al. (2003b) and O'Connor et al. (2004) showed that mid-latitude clouds most likely contain liquid if their optical depth exceeds 0.7 and the peak value of β_a from a 905 nm ceilometer is greater than $10^{-4}\,sr^{-1}\,m^{-1}$. Applying the same β_a threshold to the PE ceilometer operating at a similar wavelength, Van Tricht et al. (2014)

TCD
8, 4195–4241, 2014

showed comparable cloud optical thickness (∼ 0.5). Here we use the same threshold combined with the analysis of the case-specific cloud vertical structure to distinguish between ice and mixed-phase clouds.

3.2.2 Pyrometer: cloud base temperature

The infrared radiation pyrometer, manufactured by Heitronics Infrarot Messtechnik GmbH (Germany), is a passive radiometer measuring the downward radiance within the 8–14 µm atmospheric high-transmittance spectral window (Table 3). Atmospheric transmittance ranges from 20 % at the edges up to 80 % within the spectral window in the standard atmosphere (and even higher in Antarctica) thus minimizing the absorption due to water vapor, carbon dioxide and ozone. The pyrometer is installed in a heated wooden box with continuous lens ventilation to prevent lens contamination and blockage due to the snow.

For clouds with an emissivity approaching 1, the pyrometer temperature (T_{pyr}, °C) is determined by cloud base temperature. For optically thinner clouds, other factors, like the temperature profile and optical thickness, start playing a role. Curry and Ebert (1992) showed that in the Arctic cloud emissivity during summer approaches 1 due to frequent liquid water presence, while during the rest of the year predominantly ice clouds are observed with emissivities down to 0.2. Combination with ceilometer-derived cloud optical thickness has a potential to resolve this problem and is currently being investigated.

3.2.3 Radar: precipitation vertical profiles

The Micro Rain Radar 2 (MRR), manufactured by Meteorologische Messtechnik (METEK) GmbH (Germany), is a frequency-modulated continuous-wave (FM-CW) vertically profiling Doppler radar, transmitting at a 24 GHz frequency (λ = 1.24 cm) by a 50 mW solid state transmitter and focused by a 60 cm offset parabolic antenna (Table 4). The low power consumption of MRR makes it suitable for installation at PE and

TCD
8, 4195–4241, 2014

other remote regions where low power consumption matters. Antenna heating was not used at PE due to the inefficiency in the flushing down of the melted snow particles of rather small size and the risk of the antenna dish glaciation during the unmanned winter period. Instead, MRR was installed such that to assure natural ventilation of the antenna dish, which proved to be efficient as snowfall at PE is almost always accompanied by strong winds. Occasional formation of a thin snow layer causes no disturbance to the measurements as attenuation by dry snow is very weak at K-band (Matrosov, 2007).

Improvements to the raw signal processing in application to solid precipitation developed by Maahn and Kollias (2012) provide reliable values of radar effective reflectivity factor (Z_e, $mm^6\,m^{-3}$, expressed also in $dBz = 10\log_{10} Z_e$), mean Doppler velocity ($m\,s^{-1}$) and velocity spectral width ($m\,s^{-1}$) characterizing turbulence and variability of fall speed due to particle form and size. Useful reported precipitation profiles range from 400 m up to 3000 m a.g.l. with 100 m vertical resolution. Sensitivity down to −8 to −3 dBz, depending on range, allows MRR to detect rather weak precipitation-size particles, but is insensitive to small cloud particles. MRR sensitivity near the surface is close to the commonly used threshold of −10 dBz to identify precipitation from 35 GHz radar (Wang and Sassen, 2001). Photographs of the fallen snow crystals at PE in February 2010 and January 2011 revealed a maximum size of 0.5–0.8 mm, represented mostly by dendrites, columns, capped columns and rosettes. This is comparable to the snow particle sizes from 0.03 up to 0.6 mm measured at other Antarctic locations (Gay et al., 2002; Lachlan-Cope et al., 2001; Walden et al., 2003). Although some of the larger falling snow particles might slightly deviate from pure Rayleigh scattering at MRR wavelength (Kneifel et al., 2011), the total echo power is still dominated by the largest particles ($Z_e \sim diameter^4$ for ice, Field et al. (2005)). In addition to snowfall, MRR can also detect ice virga, defined as streaks of ice particles falling out of a cloud but evaporating before reaching the earth's surface as precipitation (AMS, 2014). Ice virga below mid-latitude altocumulus clouds is characterized by rather low number concentrations of ice crystals with particle sizes ∼0.15–0.25 mm and radar Z_e ranging between −20

TCD
8, 4195–4241, 2014

and 0 dBz (Wang et al., 2004; Westbrook and Illingworth, 2013). While MRR misses weak precipitation (virga or snowfall) with $Z_e < -8$ dBz, its sensitivity is sufficient to detect typical precipitation at the site.

Snowfall rate (S, mm w.e. h^{-1}) is calculated from hourly mean radar Z_e at 400 m a.g.l. Conversion to S is typically done using Z_e–S relationships in the form of $Z_e = aS^b$, where the coefficients a and b depend on various snowfall properties like snow particle habit, density, and snow size distribution and orientation during fall (Kulie and Bennartz, 2009; Matrosov, 2007). We apply the relationships derived by Matrosov (2007) ranging from $Z_e = 34S^{1.1}$ to $Z_e = 67S^{1.2}$ depending on particle mass and shape (see Table 1 therein). These relationships derived for "dry snow" (snowfall typically occurring at air temperatures < −8 °C characterized by unrimed snowflakes containing negligible amounts of liquid water) are expected to be most suitable for Antarctica. They are also comparable to the relationships derived by Kulie and Bennartz (2009) for three-bullet rosette and low-density spherical snow particles (Table 1 therein). The uncertainty of applying $Z_e - S$ relationships derived for 35 GHz radar to 24 GHz MRR is negligible for small snow particles (Kneifel et al., 2011) typical in Antarctica. While naturally large uncertainty exists in the derived snowfall intensity due to the chosen $Z_e - S$ relationships, here we stress the importance of the relative, rather than absolute, snowfall amount values in their relationship to the daily snow accumulation changes.

4 Results

4.1 Case studies

4.1.1 Synoptic evolution

In order to demonstrate the complementary nature of HYDRANT measurements and their utility for detailed process studies, this section presents analyses of several cases representative for different cloud and precipitation types (mixed phase clouds, ice

TCD
8, 4195–4241, 2014

clouds, ice virga, and precipitation to the surface) that occurred during the week of 6–13 February 2012. Using the European Centre for Medium-Range Weather Forecasts Interim (ERA-Interim) re-analysis data (Dee et al., 2011), local measurements are analysed in relationship to synoptic weather systems and their temporal evolution. Meteorological regime classification for each case follows the method of Gorodetskaya et al. (2013).

During the whole week of 6–13 February 2012, PE was under the influence of passing cyclones with three distinct cases characterized by various cloud and precipitation properties. Figure 2 shows the synoptic situation evolution and local weather at PE captured by the webcam (see also the Supplement for the movies produced using 1 s webcam images). The beginning of the period (on 6–7 February) was associated with a wide low pressure system centred at 65° S, 20° W (east of the Weddell Sea), and was characterized by mixed-phase stratocumulus cloud appearance at PE (Fig. 2a, case 1). On 10 February, the cyclone extended with its eastern flank reaching 30° E, while the center remained almost at the same position (68° S, 20° W). A high-pressure ridge blocking on the east was steering an intensive moisture flow into the DML resulting in two intensive snowfall events at PE (Fig. 2b, case 2). The webcam images during this case show an overcast sky and reduced visibility. Finally, on 13 February 2012 the cyclone centre moved to 8° E meridian (King Haakon VII Sea) bringing ice and mixed-phase clouds with virga and a weak snowfall to PE (Fig. 2c, case 3). The webcam image around 1:00 UTC on this day shows an arrival of overcast conditions with the "night" sun visible in a small opening at the horizon (Fig. 2c). We finish the process studies with a separate case on 8 April 2013 demonstrating a strong blowing snow event during cloud-free katabatic regime day (case 4).

4.1.2 Case 1: mixed phase clouds

On 6–7 February 2012, persistent mixed-phase stratocumulus clouds were observed over PE for almost 30 h with an important impact on radiative fluxes. Ceilometer measurements reveal a two-layer cloud structure (Fig. 3a): a thin highly reflective layer with

TCD
8, 4195–4241, 2014

$\beta_a > 10^{-4}$ sr^{-1} m^{-1}, indicating the presence of liquid, occurred at 2–2.5 km height agl, with an intermittent ice layer below ($10^{-6.5} < \beta_a < 10^{-5}$ sr^{-1} m^{-1}) extending down to 500 m a.g.l. Such mixed-phase cloud structure consisting of a liquid-containing layer on top with an ice layer below is frequently observed in mid-latitudes and in the Arctic (Gayet et al., 2009; Shupe et al., 2006; Verlinde et al., 2007; Wang et al., 2004; Westbrook and Illingworth, 2013). The lower ice part of the cloud was not detected by MRR, indicating that the ice layer was characterized by small non-precipitating particles (Fig. 3a). The mixed-phase cloud had a strong effect on T_{pyr}, which was peaking at −30 to −20 °C during the cloud presence compared to −80 °C during clear-sky periods (Fig. 3d). The highest T_{pyr} observed at around the same time (13:00 UTC) on both 6 and 7 February was associated with a liquid cloud layer, however on 6 February the liquid layer was located at lower elevation (1.8 km a.g.l.) compared to 2.5 km a.g.l. on 7 February. The extended layer of ice observed below the liquid layer on 7 February lead to a substantial increase in T_{pyr} (Fig. 3d). This variability in T_{pyr} depending on the mixed-phase cloud properties shows not only the importance of the liquid layer presence and its height, but also the potential of the ice present below the liquid layer to increase cloud LW radiative forcing.

A strong impact on surface radiative fluxes and consequently on surface and air temperature is one of the important characteristics of mixed-phase clouds over the Antarctic ice sheet. The increase in the surface incoming LW flux (LW_{in}) is tremendous: from 160 W m^{-2} during clear sky up to 240 W m^{-2} during the cloud presence. Changing cloud properties cause significant variability in the cloud radiative effect: the increase in elevation of the liquid-containing layer from 1.8 to 2.5 km a.g.l. lead to ∼20 % decrease in LW_{in} (Figs. 3a and 4a). LW_{in} was also increased due to the presence of the extended ice layer below the liquid layer on 7 February. Mixed-phase cloud reducing net SW and strongly increasing LW_{in} resulted in a rather smooth near-surface air temperature daily cycle mostly due to the warm cloudy nights (Fig. 4c).

TCD
8, 4195–4241, 2014

4.1.3 Case 2: ice/mixed-phase clouds with intensive snowfall

During 8 to 11 February 2012, ceilometer and MRR profiles (Fig. 3a–c) show cloud and precipitation properties typical of a warm frontal system passage resulting in the clear-sky noon air temperature increase by ~5 °C (Fig. 4c). First, optically thin ice cirrus clouds appear near 6 km a.g.l. in the very end of 8 February followed by arrival of mid-level clouds (possibly altrostratus) on 9 February decreasing in height and producing a virga and shortly after an intensive snowfall to the ground completely attenuating the ceilometer signal (Fig. 3a). MRR Z_e profiles show that precipitation extended at least up to 3 km a.g.l. (Fig. 3b and c). Despite the ceilometer signal attenuation by snowfall, it can be used to extend the MRR-derived precipitation profile starting at 400 m a.g.l. down to the surface. In the precipitation gap during 9 and 10 February low level mixed-phase clouds became visible, followed by another intensive and deep snowfall in the afternoon of 10 February. On 11 February, the snowfall weakened, followed by low-level virga layers and a short period of low-level ice clouds (with upper boundaries below 2 km a.g.l.) ending in a clear sky afternoon.

The T_{pyr} shows high sensitivity to cloud and precipitation occurrence (however, during snowfall signal disturbances are expected) (Fig. 3d). Appearance of thin ice clouds above 3 km a.g.l. on 8 February preceding the storm results in T_{pyr} jump up to −45 °C (Fig. 3d) with 20 W m^{-2} increase in LW_{in} (Fig. 4a). This shows the potential of the observatory to investigate the radiative importance of optically thin high-level cirrus clouds, despite the decrease of ceilometer sensitivity with height (Van Tricht et al., 2014).

The observed cloud and precipitation properties cause a large variability of LW_{in} increasing up to 255 W m^{-2} during low-level cloudiness and precipitation and an almost two-fold reduction in the net SW flux during the peak insolation hours (Fig. 4a). Periods of snowfall occurred together with intensified wind speeds and wind direction changing from southerly to easterly (Fig. 4b), which is characteristic for a synoptic weather regime. The increase of RH_i to 100 % provides an additional indication of snow present in the boundary layer (Fig. 4c). The snowfall periods were determined based on the

TCD
8, 4195–4241, 2014

MRR Z_e observations at 400 m level agl exceeding −8 dBz: from noon to midnight of 9 February for the first and 11:00 UTC 10 February to 6:00 UTC 11 February for the second snowfall event. Significant snow accumulation (up to 30 mm w.e. during the first snowfall period and 40 mm w.e. during the second snowfall) was followed by snow removal resulting in zero total accumulation over the three-day period (Fig. 4d). Snow removal was associated with strong winds with hourly mean wind speed up to 12 m s^{-1} (Fig. 4b).

4.1.4 Case 3: ice/mixed-phase clouds with virga and weak snowfall

The case on 12–14 February 2012 highlights the role of mixed-phase clouds in precipitation formation and radiative forcing. Similarly to case 2, ceilometer and MRR profiles (Figs. 3a-c) show cloud and precipitation properties typical for a warm frontal system passage: it starts with arrival of high level optically thin ice cirrus around noon of 12 February, causing an increase in T_{pyr} from −80 °C to −40 °C. Further cloud properties are somewhat different from case 2: mid-level clouds with virga last longer, with decreasing cloud base height, thickening into a low-level nimbostratus (Ns) cloud bringing weak snowfall. The Ns cloud was characterized by a geometrically thin and highly reflective layer (with $\beta_a > 10^{-4}$ sr^{-1} m^{-1}) indicating the presence of liquid at 1.5 km a.g.l. causing an increase in T_{pyr} up to −20 °C (Fig. 3d).

In the morning of 13 February, radar Z_e (Fig. 3b) shows higher vertical extent (at least up to 3 km) compared to the ceilometer β_a (Fig. 3a). The latter is attenuated by the optically and geometrically thick layer of ice virga with Z_e up to 15 dBz and Doppler velocities < 1 m s^{-1}. This is in contrast to the relatively low Z_e of the snowfall in the afternoon (< 5 dBz) and larger Doppler velocities (up to 2 m s^{-1}), indicating the presence of significantly fewer and somewhat larger particles (probably due to aggregation). Wind speed is decreasing from > 10 m s^{-1} down to negligible values in the afternoon (Fig. 4b), which have probably assisted larger Doppler velocities favoring precipitation reaching the ground.

TCD
8, 4195–4241, 2014

The hydrometeor layer after 18:00 UTC on 13 February contains precipitating ice crystals as indicated by the high radar Z_e and Doppler velocities of ~1 m s^{-1} (Figs. 3b and c). The high ceilometer β_a (Fig. 3a) could possibly be caused either by the presence of liquid within this mixed-phase cloud or by specular reflection of horizontally oriented plate crystals (Hogan et al., 2003b; Thomas et al., 1990). The fact that T_{pyr} is decreasing (Fig. 3d) supports the hypothesis of the ice dominance in this cloud system, which likely resulted in reduced emissivity. At 22:00 UTC, high β_a within a geometrically thin layer and no significant MRR signal indicate the presence of a liquid-containing cloud replaced shortly afterwards with ascending mid-level ice layers (Fig. 3a). With the appearance of this short-lived thin highly reflective layer, T_{pyr} increases again to −20 °C supporting the presence of liquid water with cloud emissivity probably approaching 1, and counteracting the effect of the 1 km increase in the cloud base height (Fig. 3a and d).

Changing cloud properties exhibit a strong influence on LW_{in} (as high as 240–260 W m^{-2} during cloudy conditions, Fig. 4a). Near-surface air temperature is nearly constant at −10 °C during the entire day (Fig. 4c). During the snowfall event at 16:00 UTC, easterly winds up to 10 m s^{-1} slow down and change to southerly direction (Fig. 4b). Such wind behaviour demonstrates a transition from a synoptic regime (a storm under cyclonic influence) to a katabatic regime (southerly flow from the Antarctic interior with rather quiet wind speeds due to the mountain sheltering, Gorodetskaya et al., 2013). Small snow height variability throughout the day is associated with wind deposition/removal (in the absence of snowfall to the ground) and showing insignificant accumulation of snow after the snowfall event (Fig. 4d).

4.1.5 Case 4: cloud-free sky blowing snow

A special case on 8 April 2013 shows a strong blowing snow event occurring during cloudless conditions, which is a rare and extreme event at PE, where katabatic winds are usually rather weak being sheltered by the mountain range (Gorodetskaya et al., 2013; Thiery et al., 2012). The webcam movies during the daylight confirm clear sky

TCD
8, 4195–4241, 2014

conditions and show a strong drifting/blowing snow event (see the Supplement). In order to capture the details of the event, raw ceilometer β_a profiles were investigated (Fig. 5a). The noise reduction and averaging used for cloud and precipitation recognition (PT algorithm, Van Tricht et al., 2014), removes most of the clear-sky blowing snow layers and is not applied for this case. Figure 5a shows snow particle presence in the lowest 100 m in the beginning of the day with the blowing snow layer increasing progressively during the day together with the increase in wind speeds (Fig. 5b). The peak of the blowing snow layer height up to 500 m occurs at 21:00–22:00 UTC when the hourly mean wind speed increases up to 21 m s^{-1}. Low LW_{in} values observed during this day (140 W m^{-2}, Fig. 5b) are representative of a cold katabatic regime with clear-sky conditions (Gorodetskaya et al., 2013). The observed wind speeds by large exceed the threshold (>8 m s^{-1}) needed for lifting snow from the ground up to significant heights according to observational and modeling studies (Bintanja, 1998; Leonard et al., 2012).

MRR detects no signal during this day, which confirms that the blowing snow is limited to a shallow layer near the surface (<500 m a.g.l.), while precipitation is expected to originate from much higher layers (Fig. 3b). Thus, the ceilometer signal in the near-surface layers combined with low LW_{in} values, high near-surface wind speeds and absence of the MRR signal, can be used to distinguish blowing/drifting snow events from snow falling from a cloud. Here we show only one example; further analysis applied to longer time series and also to other ceilometer locations can produce valuable statistics on the clear-sky blowing snow heights, needed for evaluation of the satellite-derived blowing snow events (Palm et al., 2011).

4.2 Statistics of cloud and precipitation properties

4.2.1 Combining ceilometer and radar profiles

In addition to case studies, we provide a compilation of fundamental cloud and precipitation statistics derived from the remote-sensing instruments based on the available

TCD
8, 4195–4241, 2014

measurement periods during 2010–2013 (14 months for cloud measurements mainly in summer/autumn and 26 months of snowfall measurements including an entire year, see Table 1 for exact measurement periods for each instrument). First, ceilometer β_a profiles were processed to exclude noise and clear sky values using the PT algorithm as described by Van Tricht et al. (2014). This allowed isolation of the profiles with cloud and/or precipitation at the original 15 s temporal resolution. Further, β_a profiles were averaged over 1 min and collocated with MRR Z_e profiles. Finally, cloudy profiles with snowfall were identified using a condition $Z_e > -8$ dBz at 400 m a.g.l. continuously during 10 min. Cloudy profiles with liquid were detected using a threshold of 10^{-4} sr^{-1} m^{-1} applied to β_a profiles without snowfall.

Figure 6 shows the frequency by height for Z_e and β_a demonstrating the typical cloud and precipitation signal intensities observed at PE and their distribution with height. Precipitation intensity near the surface (400 m a.g.l.) is most frequent within $-5 < Z_e < 12$ dBz narrowing upwards to $-2 < Z_e < 8$ dBz at 2500 m a.g.l. (Fig. 6a). The tendency towards higher minimum Z_e values with height can be related to the decrease of MRR sensitivity with height (Maahn and Kollias, 2012). Precipitation of 1 mm hr^{-1} is commonly used as a threshold between "light" and "moderate" precipitation intensities (Rasmussen et al., 1999). It corresponds to 15–18 dBz according to the range of $Z_e - S$ relationships for dry snow (see Sect. 3.2.3). Using the lower bound (Z_e = 15 dBz at 400 m a.g.l. range) as a threshold, PE is characterized overall by low intensity precipitation (94 % of total precipitation time) with rare occasional moderate intensity snowfalls (6 % of precipitation). Most of precipitation is confined within the first 2.5 km a.g.l., while moderate intensity precipitation is limited to 2 km a.g.l.

The frequency by height diagram for ceilometer β_a was first constructed for all cloudy profiles (Fig. 6b). Decreasing with height frequency of occurrence for the low β_a values can be related, as for the radar, to the decreasing sensitivity of ceilometer with height (Van Tricht et al., 2014). The most frequently observed backscatter signal is found within $10^{-5.5} < \beta_a < 10^{-4.5}$ sr^{-1} m^{-1}, observed from near the surface up to 3 km a.g.l. The nearest to the surface layers (below 500 km a.g.l.) are characterized by rather high

TCD
8, 4195–4241, 2014

backscatter (most frequently within $10^{-5} < \beta_a < 10^{-4}\,sr^{-1}\,m^{-1}$) and can be a signature of both clouds and precipitation to the ground. Excluding snowfall profiles from the analysis shows clearly that these high β_a values near the surface are related to snowfall (Fig. 6c). Cloudy profiles without snowfall show the highest frequency between 500 and 3 km a.g.l. (Fig. 6c). Low β_a values ($< 10^{-5}\,sr^{-1}\,m^{-1}$) dominate the layers below 1 km a.g.l. and are characteristic of ice layers extending down to the surface, which can be both cloud ice layers or light precipitation beyond the MRR sensitivity. Backscatter values larger than $10^{-4}\,sr^{-1}\,m^{-1}$, which we can more certainly relate now to the liquid-containing cloud layers, are confined within the height interval between 1 and 3 km a.g.l.

As shown by Van Tricht et al. (2014), 80 % of all clouds and precipitation layers at PE have base heights below 2 km a.g.l., while the majority (78 %) of the optically thick liquid-containing clouds have their bases between 1 and 3 km a.g.l. Combining these results with Fig. 6c points to a large vertical range of ice clouds. At the same time, the ability of the ceilometer to detect the vertical extent of the mixed phase clouds is limited due to the fast attenuation of ceilometer signal by the liquid-containing layers (e.g., Platt et al., 1994). In addition, the rapid ceilometer signal attenuation makes it unsuitable for detection of multiple liquid-containing layers.

4.2.2 Cloud and snowfall occurrence frequency

Using collocated 1 min β_a and Z_e values, we calculated hourly cloud occurrence frequency (COF), snowfall occurrence frequency (SOF) and liquid cloud occurrence frequency (LCOF) distributions. Hourly COF is a metric generally used to express cloud cover based on point measurements in time (e.g., Town et al., 2007). Here it is expressed as a unitless fraction (0–1) to distinguish from the COF distribution frequency given in % (similarly for SOF and LCOF, see Fig. 7). Cloudiness at PE is strongly bimodal with the majority of the time being either clear sky or overcast (Fig. 7). Overcast conditions for all types of clouds and precipitation were observed 35 % of the measure-

TCD
8, 4195–4241, 2014

ment period. Due to the presence of partial cloudiness, mean COF including all clouds and precipitation for the entire measurement period is 0.46.

Further, the overcast conditions are divided among liquid-containing clouds (7 % of the total measurement period or 20 % of the overcast periods), snowfall (6 % of the total period or 17 % of the overcast), and ice clouds or weak precipitation not detected by MRR (22 % of the total period or 63 % of the overcast). Thus, while ice clouds occur most frequently, mixed-phase clouds are also observed during a significant period of time. Low SOF, compared to cloudy periods, combined with precipitation intensity statistics (Fig. 6a), indicates once more the importance of occasional intensive snowfall events. It should be noted that SOF was estimated only for the periods when cloud data were available (summer-autumn months), thus excluding the winter snowfall measurements during 2012 (which are included in Fig. 6a).

4.2.3 Snowfall and accumulation

Further, we show the role of the snowfall-driven high accumulation events in the local surface mass budget. PE site is characterized by high interannual variability in local snow accumulation (230, 23, 227, and 52 mm w.e. during 2009, 2010, 2011, and 2012, respectively), which is in accordance with the yearly 180 km long stake line measurements from PE to the coast (GLACIOCLIM project, Favier et al., 2013): averaged over all stakes yearly total accumulation is 606, 157, and 598 mm w.e. for 2009, 2010, and 2011, respectively). PE AWS measurements clearly show the anomalous accumulation observed over entire DML in 2009 and 2011 (Boening et al., 2012; Lenaerts et al., 2013). Net snow accumulation is determined by several processes, including precipitation, sublimation/deposition, removal and deposition of snow by wind, and melt (in the coastal areas of the ice sheet) (Van den Broeke et al., 2004). While precipitation is the major positive component of the surface mass budget, it is difficult to disentangle the contribution of precipitation from continuous wind-driven snow deposition and erosion. Here we use radar-derived snowfall rates collocated with snow height changes from

TCD
8, 4195–4241, 2014

AWS in order to distinguish accumulation due to snowfall from accumulation due to the wind deposition.

We analysed two years (2011–2012) of snow height changes together with daily mean snowfall rate values (Fig. 8). Each year is punctuated by 7–8 high accumulation events (defined as days with accumulation $> 10\,\mathrm{mm\,w.e.\,day^{-1}}$). Comparing the two years, 2011 and 2012, shows that the magnitude of these occasional high accumulation events determines the difference in the total annual accumulation. We find that all of these high-accumulation events (indicated with blue circles in Fig. 8) are associated with snowfall of various intensity (blue diamonds). The three most intensive snowfalls, leading to the largest daily snow accumulation, occurred during 2011 (14–17 February, 16–17 December and 19–20 December), and were associated with exceptional moisture transport towards East Antarctica organized into so-called atmospheric rivers (Gorodetskaya et al., 2014). It should be noted that during the winter 2011, the attribution of exceptionally high accumulation events to snowfall was unfortunately not possible due to the radar measurements gap. Despite the differences in snowfall intensity and uncertainties in $Z_e - S$ relationships, radar measurements allow to directly associate high snow accumulation events with snowfall. The occasional nature of snowfalls and associated step-wise snow height changes, necessitate fine temporal resolution measurements demonstrated both by MRR (averaged to 1 min) and an acoustic snow height ranger (1 h).

At the same time, small and medium accumulation events could be both due to snowfall and wind-driven deposition (Fig. 8). Also, some intensive snowfall events result in zero net snow accumulation due to the snow removal by strong winds under cyclonic conditions. During the winter of 2012, for example, snowfall was observed rather frequently, resulting in no significant snow height changes (Fig. 8). This was also observed during case 2, when rather long and intensive snowfall (Fig. 3b) accompanied by high wind speeds (Fig. 4b) resulted in zero net snow accumulation (Fig. 4d). In addition to the snow transport and redistribution by the wind, snow mass can be also removed by surface and drifting snow sublimation. While both surface and drifting snow sublimation

TCD
8, 4195–4241, 2014

are rather small at PE removing together about 10 % of snow (Thiery et al., 2012), it can be substantial at other locations especially in the escarpment zone of the plateau with high katabatic winds (Gallée et al., 2001; Lenaerts et al., 2012a; Thiery et al., 2012).

5 Conclusions and outlook

In this paper we present a new cloud-precipitation-meteorological observatory established in the escarpment zone of eastern Dronning Maud Land, East Antarctica. Cloud and precipitation properties at high vertical and temporal resolution are derived from a set of ground-based remote sensing instruments (910 nm ceilometer, 8–14 µm radiation pyrometer, and 24 GHz vertically profiling precipitation radar). These are combined with automatic weather station measurements of near-surface meteorology and radiative fluxes, as well as local snow height changes.

The paper demonstrates the value of this set of instruments via detailed case studies and presents important cloud and precipitation properties based on the available measurement periods during 2010–2013 (14 months for cloud measurements and 26 months of snowfall measurements). Case studies show the ability of the observatory to capture complex and constantly evolving cloud and precipitation properties, as well as to measure intensive wind-driven blowing snow events. In particular, we have shown that the observatory can be used for investigating the following relationships:

- distinguish between ice clouds (including weak precipitation), virga (precipitation not reaching the surface), mixed-phase clouds, and snowfall;
- study the effect of changing cloud base heights and temperatures on surface radiative fluxes;
- separately estimate impact of the mixed-phase clouds, their changing height and structure (such as presence of an ice layer below), on the surface radiative fluxes;

TCD
8, 4195–4241, 2014

- assess the vertical extent and radiative forcing of thin ice clouds;
- using collocated ceilometer and MRR profiles, assure that radar-derived snowfall (limited to 400 m a.g.l.) is observed all the way to the surface;
- distinguish snow accumulation due to snowfall from wind-driven deposition;
- identify intensive (> 10 m a.g.l.) wind-driven blowing snow events during cloud-free conditions.

Statistical analysis using ceilometer and MRR synergies and based on the available measurement periods during 2010–2013, reveals cloud and precipitation properties, many of which are derived for the first time over the Antarctic ice sheet. Ice clouds and weak precipitation are most frequently found from near the surface up to 3–3.5 km a.g.l., while the lowest observed liquid-containing clouds are confined to 1–3 km a.g.l. Clouds at PE show a clear bimodal distribution with either clear sky or overcast most of the time. While ice clouds occur most frequently, as expected in the polar regions, mixed-phase clouds are also observed during a significant period of time (20 % of all cloudy overcast cases). Snowfall rates derived from radar measurements show high frequency of low intensity precipitation with rare occasional moderate intensity snowfalls of > 1 mm w.e. h^{-1} (observed 6 % of the total precipitation period).

Another long-standing question, which can be addressed using the observatory data, is attribution of accumulation to snowfall in contrast to the wind-driven deposition. Despite the MRR limitation to vertical profiling, its high temporal resolution together with typically large-scale and occasional nature of synoptic-driven precipitation allows capture of all major precipitation events contributing to the local surface mass budget. Large local accumulation events (> 10 mm w.e. day^{-1}), responsible for the majority of the total annual surface mass budget, are all attributed to occasional snowfall of various intensity (during the period of snowfall measurements). In contrast to the large accumulation events, medium to low accumulation occur both due to snowfall and wind-driven deposition. Also not every snowfall results in significant snow accumulation, and

TCD
8, 4195–4241, 2014

wind erosion (together with sublimation) can entirely remove locally precipitated snow mass. Attribution of accumulation to snowfall is important not only for understanding the hydrologic cycle processes and mechanisms behind surface mass budget, but also for paleoclimate record interpretation (Masson-Delmotte et al., 2008; Schlosser et al., 2010).

Application of the observatory extends beyond cloud and precipitation, and can be used to capture intensive wind-driven blowing snow events (in the absence of snowfall from clouds) up to several hundred meters above the ground, associated with strong near-surface winds. Palm et al. (2011) applied a new technique of detecting clear-sky blowing snow events using satellite-based lidar data and found an average depth of 120 m and a maximum of 1 km for all detected blowing snow events. Measurements from the ceilometer installed at PE and also ceilometers found at other locations around Antarctica can be used for evaluation of the satellite-derived large-scale blowing snow events.

The goal of the observatory is to evaluate clouds and precipitation simulated by climate models allowing both detailed look into processes and statistical comparisons. It can be also used in synergy with satellite cloud and precipitation data. Collocating profiles from ground-based and satellite lidars can offer better representation of the cloud vertical structure. Similarly, collocation of MRR precipitation measurements with satellite-based radar provides additional information on precipitation occurrence and properties close to the surface offering a solution to the disturbance of satellite radars due to ground-clutter (Maahn et al., 2014). Even though the instrument setup is much less sophisticated compared to mid-latitude observational supersites (e.g., Atmospheric Radiation Measurement research facilities), the combination of basic lidar, radar and passive infrared instruments, together with meteorological and snow accumulation measurements, already allows a number of important cloud and precipitation properties to be derived, and could be easily installed at other Antarctic stations.

TCD
8, 4195–4241, 2014

The Supplement related to this article is available online at doi:10.5194/tcd-8-4195-2014-supplement.

Acknowledgements. This project has been successful thanks to continuous support of many people, companies and institutions. We are grateful to the Belgian Science Policy (BELSPO) for the financial support of the HYDRANT project (EA/01/04AB). We thank International Polar Foundation (IPF) and all staff at Princess Elisabeth base for providing the infrastructure, technical and logistical support. We are thankful to Alexander Mangold (Royal Meteorological Institute of Belgium) for his continuous help with onsite instrument maintenance, together with IPF engineer Eric Verhagen. Special thanks for continuous technical support of the KU Leuven engineers Jos Meersmans and Valentijn Tuts, and all companies who provided the remote-sensing instruments and technical support – Vaisala (Finland), Heitronics/MeraBenelux (Germany/Netherlands), Metek (Germany), and Mobotix (Germany). Special thanks to Johan Boon and Hilde Vandenhoeck (KU Leuven) for computer and website support. We are grateful to Carleen Reijmer and Wim Boot (Institute for Marine and Atmospheric research Utrecht, the Netherlands) for the AWS technical support and raw data processing. We are grateful to Roland Meister (Institute for Snow and Avalanche Research – SLF, Switzerland) for providing the equipment and training for snow pit measurements. We thank Glacioclim-SAMBA project (France), IPF and Vincent Favier (Laboratoire de Glaciologie et Géophysique de l'Environnement, France) for providing stake-line snow measurements. We thank colleagues from the Regional Climate Studies group at KU Leuven for their support and feedback. IG was funded by the BELSPO grant EA/01/04AB; MM was supported by the project ADMIRARI II of the German Research Association (DFG) under research grant number LO901/5-1; KVT was supported by the Belgian Research Foundation Flanders (FWO) PhD fellowship. Part of the University of Cologne contribution was performed at the Hans-Ertel Centre for Weather Research – Climate Monitoring Branch funded by the Federal Ministry of Transport, Building and Urban Development (BMVBS) of Germany.

References

American Meteorological Society: Virga. Glossary of Meteorology, available at: http://glossary.ametsoc.org/wiki/Virga, last access: 23 July 2014. 4205

TCD
8, 4195–4241, 2014

Arctowski, H.: Aperçu des resultats meteorologiques de l'hivernage Antarctique de la "Belgica", Ann. Met. Observ. Roy. Belg. (Bruxelles), 267, available at: http://docs.lib.noaa.gov/rescue/IPY/ipy_004_pdf/Qc9949a731904.pdf (last access: 5 June 2014), 1904. 4199

Averianov, V. G.: Glyatsio-klimatologiya Antarktidy [Glacio-climatology of Antarctic], Gidrometeoizdat, Leningrad, 197 p., 1990. 4200

Bennartz, R., Shupe, M. D., Turner, D. D., Walden, V. P., Steffen, K., Cox, C. J., Kulie, M. S., Miller, N. B., and Pettersen, C.: July 2012 Greenland melt extent enhanced by low-level liquid clouds, Nature, 496, 83–86, doi:10.1038/nature12002, 2013. 4197

Berque, J., Lubin, D., and Somerville, R. C. J.: Transect method for Antarctic cloud property retrieval using AVHRR data, Int. J. Remote Sens., 32, 2887–2903, doi:10.1080/01431161003745624 2011. 4200

Bintanja, R.: The contribution of snowdrift sublimation to the surface mass balance of Antarctica, Ann. Glaciol., 27, 251–259, 1998. 4212

Bintanja, R. and Van den Broeke, M. R.: The influence of clouds on the radiation budget of ice and snow surfaces in Antarctica and Greenland in summer, Int. J. Climatol., 16, 1281–1296, 1996. 4197

Boening, C., Lebsock, M., Landerer, F., and Stephens, G.: Snowfall-driven mass change on the East Antarctic ice sheet, Geophys. Res. Lett., 39, L21501, doi:10.1029/2012GL053316, 2012. 4215

Bromwich, D. H., Nicolas, J. P., Hines, K. M., Kay, J. E., Key, E. L., Lazzara, M. A., Lubin, D., McFarquhar, G. M., Gorodetskaya, I. V., Grosvenor, D. P., Lachlan-Cope, T., and Van Lipzig, N. P. M.: Tropospheric clouds in Antarctica, Rev. Geophys., 50, RG1004, doi:10.1029/2011RG000363, 2012. 4197, 4199, 4200

Bryazgin, N. N.: Atmosfernye osadki v Antarktide i ih mnogoletnyaa izmenchivost' [Atmospheric precipitation in Antarctica and its inter-annual variability] // Meteorol. Issled. v Antarktike – Part I, Gidrometeoizdat, Leningrad, 30–34, 1990. 4200

Colle, B. A., Stark, D., and Yuter, S. E.: Surface microphysical observations within east coast winter storms on Long Island, NY, Mon. Weather Rev., doi:10.1175/MWRD-14-00035.1, in press, 2014. 4202

Curry, J. A. and Ebert, E. E.: Annual cycle of radiation fluxes over the Arctic Ocean: sensitivity to cloud optical properties, J. Climate, 5, 1267–1280, doi:10.1175/1520-0442(1992)005<1267:ACORFO>2.0.CO;2, 1992. 4204

TCD
8, 4195–4241, 2014

Das, I., Bell, R. E., Scambos, T. A., Wolovick, M., Creyts, T. T., Studinger, M., Frearson, N., Nicolas, J. P., Lenaerts, J. T. M., and Van den Broeke, M. R.: Influence of persistent wind scour on the surface mass balance of Antarctica, Nat. Geosci., 6, 367–371, doi:10.1038/ngeo1766, 2013. 4198

Dee, D. P., Uppala, S. M., Simmons, A. J., Berrisford, P., Poli, P., Kobayashi, S., Andrae, U., Balmaseda, M. A., Balsamo, G., Bauer, P., Bechtold, P., Beljaars, A. C. M., van de Berg, L., Bidlot, J., Bormann, N., Delsol, C., Dragani, R., Fuentes, M., Geer, A. J., Haimberger, L., Healy, S. B., Hersbach, H., Hólm, E. V., Isaksen, L., Kå llberg, P., Köhler, M., Matricardi, M., McNally, A. P., Monge-Sanz, B. M., Morcrette, J.-J., Park, B.-K., Peubey, C., de Rosnay, P., Tavolato, C., Thépaut, J.-N., and Vitart, F.: The ERA-interim reanalysis: configuration and performance of the data assimilation system, Q. J. Roy. Meteorol. Soc., 137, 553–597, doi:10.1002/qj.828, 2011. 4207

Del Guasta, M., Morandi, M., Stefanutti, L., Brechet, J., and Piquad, J.: One year of cloud lidar data from Dumont d'Urville (Antarctica): 1. General overview of geometrical and optical properties, J. Geophys. Res., 98, 18575, doi:10.1029/93JD01476, 1993. 4200

Favier, V., Agosta, C., Parouty, S., Durand, G., Delaygue, G., Gallée, H., Drouet, A.-S., Trouvilliez, A., and Krinner, G.: An updated and quality controlled surface mass balance dataset for Antarctica, The Cryosphere, 7, 583–597, doi:10.5194/tc-7-583-2013, 2013. 4215

Field, P. R., Hogan, R. J., Brown, P. R. A., Illingworth, A. J., Choularton, T. W., and Cotton, R. J.: Parametrization of ice-particle size distributions for mid-latitude stratiform cloud, Q. J. Roy. Meteorol. Soc., 131, 1997–2017, doi:10.1256/qj.04.134, 2005. 4205

Frezzotti, M., Urbini, S., Proposito, M., Scarchilli, C., and Gandolfi, S.: Spatial and temporal variability of surface mass balance near Talos Dome, East Antarctica, J. Geophys. Res., 112, F02032, doi:10.1029/2006JF000638, 2007. 4198

Frezzotti, M., Scarchilli, C., Becagli, S., Proposito, M., and Urbini, S.: A synthesis of the Antarctic surface mass balance during the last 800 yr, The Cryosphere, 7, 303–319, doi:10.5194/tc-7-303-2013, 2013. 4198

Gallée, H. and Gorodetskaya, I. V.: Validation of a limited area model over Dome C, Antarctic Plateau, during winter, Clim. Dynam., 34, 61–72, doi:10.1007/s00382-008-0499-y, 2010. 4199

Gallée, H., Guyomarch, G., and Brun, E.: Impact of snow drift on the antarctic ice sheet surface mass balance: possible sensitivity to snow-surface properties, Bound.-Lay. Meteorol., 99, 1–19, 2001. 4217

TCD
8, 4195–4241, 2014

Gay, M., Fily, M., Genthon, C., Frezzotti, M., Oerter, H., and Winther, J.-G.: Snow grain-size measurements in Antarctica, J. Glaciol., 48, 527–535, doi:10.3189/172756502781831016, 2002. 4205

Gayet, J.-F., Mioche, G., Dörnbrack, A., Ehrlich, A., Lampert, A., and Wendisch, M.: Microphysical and optical properties of Arctic mixed-phase clouds. The 9 April 2007 case study., Atmos. Chem. Phys., 9, 6581–6595, doi:10.5194/acp-9-6581-2009, 2009. 4208

Girard, E. and Blanchet, J.-P.: Simulation of Arctic diamond dust, ice fog, and thin stratus using an explicit aerosol–cloud–radiation model, J. Atmos. Sci., 58, 1199–1221, doi:10.1175/1520-0469(2001)058<1199:SOADDI>2.0.CO;2, 2001. 4197

Gorodetskaya, I. V., Van Lipzig, N. P. M., Van den Broeke, M. R., Mangold, A., Boot, W., and Reijmer, C. H.: Meteorological regimes and accumulation patterns at Utsteinen, Dronning Maud Land, East Antarctica: analysis of two contrasting years, J. Geophys. Res.-Atmos., 118, 1700–1715, doi:10.1002/jgrd.50177, 2013. 4198, 4201, 4202, 4207, 4211, 4212

Gorodetskaya, I. V., Tsukernik, M., Claes, K., Ralph, F. M., Neff, W. D., and van Lipzig, N. P. M.: The role of atmospheric rivers in anomalous snow accumulation in East Antarctica, Geophys. Res. Lett., in review, 2014. 4216

Gregory, J. M. and Huybrechts, P.: Ice-sheet contributions to future sea-level change, Philos. T. Roy. Soc. A, 364, 1709–31, doi:10.1098/rsta.2006.1796, 2006. 4197

Grenier, P., Blanchet, J. P., and Muñoz-Alpizar, R.: Study of polar thin ice clouds and aerosols seen by CloudSat and CALIPSO during midwinter 2007, J. Geophys. Res.-Atmos., 114, D09201, doi:10.1029/2008JD010927, 2009. 4197, 4200

Groot Zwaaftink, C. D., Cagnati, A., Crepaz, A., Fierz, C., Macelloni, G., Valt, M., and Lehning, M.: Event-driven deposition of snow on the Antarctic Plateau: analyzing field measurements with SNOWPACK, The Cryosphere, 7, 333–347, doi:10.5194/tc-7-333-2013, 2013. 4198

Hahn, C. J. and Warren, S. G.: Cloud Climatology for Land Stations Worldwide, 1971–1996, Tech. rep., NDP-026D, Carbon Dioxide Information Analysis Center, Oak Ridge National Laboratory, Oak Ridge, TN, doi:10.3334/CDIAC/cli.ndp026d, 2003. 4200

Henderson, D. S., L'Ecuyer, T., Stephens, G., Partain, P., and Sekiguchi, M.: A multisensor perspective on the radiative impacts of clouds and aerosols, J. Appl. Meteorol. Clim., 52, 853–871, doi:10.1175/JAMC-D-12-025.1, 2013. 4200

TCD
8, 4195–4241, 2014

Hogan, R. J., Francis, P. N., Flentje, H., Illingworth, A. J., Quante, M., and Pelon, J.: Characteristics of mixed phase clouds. Part I: Lidar, radar and aircraft observations from CLARE '98, Quart. J. Roy. Meteor. Soc, 129, 2089–2116, doi:10.1256/qj.01.208, 2003a. 4198

Hogan, R. J., Illingworth, A. J., O'Connor, E. J., and PoiaresBaptista, J. P. V.: Characteristics of mixed-phase clouds. II: A climatology from ground-based lidar, Q. J. Roy. Meteorol. Soc., 129, 2117–2134, doi:10.1256/qj.01.209, 2003b. 4203, 4211

IPCC: Climate Change 2013: the Physical Science Basis. Contribution of Working Group I to the Fifth Assessment Report of the Intergovernmental Panel on Climate Change., available at: http://www.climatechange2013.org/ (last access: 2 June 2014), 2013. 4197

Kneifel, S., Maahn, M., Peters, G., and Simmer, C.: Observation of snowfall with a low-power FM-CW K-band radar (micro rain radar), Meteorol. Atmos. Phys., 113, 75–87, doi:10.1007/s00703-011-0142-z, 2011. 4202, 4205, 4206

Krinner, G., Magand, O., Simmonds, I., Genthon, C., and Dufresne, J. L.: Simulated Antarctic precipitation and surface mass balance at the end of the twentieth and twenty-first centuries, Clim. Dynam., 28, 215–230, doi:10.1007/s00382-006-0177-x, 2007. 4197

Kuipers Munneke, P., Reijmer, C. H., and van den Broeke, M. R.: Assessing the retrieval of cloud properties from radiation measurements over snow and ice, Int. J. Climatol., 31, 756–769, doi:10.1002/joc.2114, 2011. 4200

Kulie, M. S. and Bennartz, R.: Utilizing spaceborne radars to retrieve dry snowfall, J. Appl. Meteorol. Clim., 48, 2564–2580, doi:10.1175/2009JAMC2193.1, 2009. 4206

Lachlan-Cope, T.: Antarctic clouds, Polar Res., 29, 150–158, doi:10.1111/j.1751-8369.2010.00148.x, 2010. 4198, 4200

Lachlan-Cope, T., Ladkin, R., Turner, J., and Davison, P.: Observations of cloud and precipitation particles on the Avery Plateau, Antarctic Peninsula, Antarct. Sci., 13, 339–348, doi:10.1017/S0954102001000475, 2001. 4205

Lampert, A., Ehrlich, A., Dörnbrack, A., Jourdan, O., Gayet, J.-F., Mioche, G., Shcherbakov, V., Ritter, C., and Wendisch, M.: Microphysical and radiative characterization of a subvisible midlevel Arctic ice cloud by airborne observations – a case study, Atmos. Chem. Phys., 9, 2647–2661, doi:10.5194/acp-9-2647-2009, 2009. 4197

Lazzara, M. A., Keller, L. M., Stearns, C. R., Thom, J. E., and Weidner, G. A.: Antarctic Satellite Meteorology: Applications for Weather Forecasting, Mon. Weather Rev., 131, 371–383, doi:10.1175/1520-0493(2003)131<0371:ASMAFW>2.0.CO;2, 2003. 4200

TCD
8, 4195–4241, 2014

Lenaerts, J. T., Van Den Broeke, M. R., Scarchilli, C., and Agosta, C.: Impact of model resolution on simulated wind, drifting snow and surface mass balance in Terre Adélie, East Antarctica, J. Glaciol., 58, 821–829, doi:10.3189/2012JoG12J020, 2012a. 4198, 4217

Lenaerts, J. T. M., van den Broeke, M. R., van de Berg, W. J., van Meijgaard, E., and Kuipers Munneke, P.: A new, high-resolution surface mass balance map of Antarctica (1979–2010) based on regional atmospheric climate modeling, Geophys. Res. Lett., 39, L04501, doi:10.1029/2011GL050713, 2012b. 4198

Lenaerts, J. T. M., van Meijgaard, E., van den Broeke, M. R., Ligtenberg, S. R. M., Horwath, M., and Isaksson, E.: Recent snowfall anomalies in Dronning Maud Land, East Antarctica, in a historical and future climate perspective, Geophys. Res. Lett., 40, 2684–2688, doi:10.1002/grl.50559, 2013. 4215

Leonard, K. C., Tremblay, L. B., Thom, J. E., and MacAyeal, D. R.: Drifting snow threshold measurements near McMurdo station, Antarctica: A sensor comparison study, Cold Reg. Sci. Technol., 70, 71–80, doi:10.1016/j.coldregions.2011.08.001, 2012. 4212

Ligtenberg, S. R. M., van de Berg, W. J., van den Broeke, M. R., Rae, J. G. L., and van Meijgaard, E.: Future surface mass balance of the Antarctic ice sheet and its influence on sea level change, simulated by a regional atmospheric climate model, Clim. Dynam., 41, 867–884, doi:10.1007/s00382-013-1749-1, 2013. 4197

Liston, G. E., Bruland, O., Winther, J.-G., Elvehø, H., and Knut, S.: Meltwater production in Antarctic blue-ice areas: sensitivity to changes in atmospheric forcing, Polar Res., 18, 283–290, doi:10.1111/j.1751-8369.1999.tb00305.x, 1999. 4197

Maahn, M. and Kollias, P.: Improved Micro Rain Radar snow measurements using Doppler spectra post-processing, Atmos. Meas. Tech., 5, 2661–2673, doi:10.5194/amt-5-2661-2012, 2012. 4202, 4205, 4213

Maahn, M., Burgard, C., Crewell, S., Gorodetskaya, I. V., Kneifel, S., Lhermitte, S., Van Tricht, K., and Van Lipzig, N. P. M.: How does the space-borne radar blind-zone affect derived surface snowfall statistics in polar regions?, J. Geophys. Res., in review, 2014. 4219

Masson-Delmotte, V., Hou, S., Ekaykin, A., Jouzel, J., Aristarain, A., Bernardo, R. T., Bromwich, D., Cattani, O., Delmotte, M., Falourd, S., Frezzotti, M., Gallée, H., Genoni, L., Isaksson, E., Landais, A., Helsen, M. M., Hoffmann, G., Lopez, J., Morgan, V., Motoyama, H., Noone, D., Oerter, H., Petit, J. R., Royer, A., Uemura, R., Schmidt, G. A., Schlosser, E., Simões, J. C., Steig, E. J., Stenni, B., Stievenard, M., van den Broeke, M. R., van de Wal, R. S. W., van de Berg, W. J., Vimeux, F., and White, J. W. C.: A review of antarctic

TCD
8, 4195–4241, 2014

surface snow isotopic composition: observations, atmospheric circulation, and isotopic modeling*, J. Climate, 21, 3359–3387, doi:10.1175/2007JCLI2139.1, 2008. 4219
Matrosov, S. Y.: Modeling backscatter properties of snowfall at millimeter wavelengths, J. Atmos. Sci., 64, 1727–1736, doi:10.1175/JAS3904.1, 2007. 4205, 4206
Mohn, H.: Roald Amundsen's Antarctic expedition scientific results. Meteorology. (Videnskapsselskapets Skrifter. I. Mat.-Naturv. Klasse 1915. No. 5), Tech. rep., Kristiania, I. Kommission Hos Jacob Dybwad, available at: http://docs.lib.noaa.gov/rescue/IPY/IPY_020_pdf/Qc9949M641915.pdf (last access: 23 July 2014), 1915. 4200
Morley, B. M., Uthe, E. E., and Viezee, W.: Airborne lidar observations of clouds in the Antarctic troposphere, Geophys. Res. Lett., 16, 491–494, doi:10.1029/GL016i006p00491, 1989. 4200
Morrison, H. and Pinto, J. O.: Mesoscale modeling of springtime Arctic mixed-phase stratiform clouds using a new two-moment bulk microphysics scheme, J. Atmos. Sci., 62, 3683–3704, doi:10.1175/JAS3564.1, 2005. 4198
Münkel, C., Eresmaa, N., Räsänen, J., and Karppinen, A.: Retrieval of mixing height and dust concentration with lidar ceilometer, Bound.-Lay. Meteorol., 124, 117–128, doi:10.1007/s10546-006-9103-3, 2006. 4203
O'Connor, E., Illingworth, A., and Hogan, R.: A Technique for Autocalibration of Cloud Lidar, J. Atmos. Ocean. Tech., 21, 777–786, doi:10.1175/1520-0426(2004)021<0777:ATFAOC>2.0.CO;2, 2004. 4203
Pal, S. R., Steinbrecht, W., and Carswell, A. I.: Automated method for lidar determination of cloud-base height and vertical extent, Appl. Optics, 31, 1488–94, doi:10.1364/AO.31.001488, 1992. 4203
Palm, S. P., Yang, Y., Spinhirne, J. D., and Marshak, A.: Satellite remote sensing of blowing snow properties over Antarctica, J. Geophys. Res., 116, D16123, doi:10.1029/2011JD015828, 2011. 4212, 4219
Pattyn, F., Matsuoka, K., and Berte, J.: Glacio-meteorological conditions in the vicinity of the Belgian Princess Elisabeth Station, Antarctica, Antarct. Sci., 22, 79–85, doi:10.1017/S0954102009990344, 2009. 4201
Platt, C. M., Young, S. A., Carswell, A. I., Pal, S. R., McCormick, M. P., Winker, D. M., DeGuasta, M., Stefanutti, L., Eberhard, W. L., Hardesty, M., Flamant, P. H., Valentin, R., Forgan, B., Gimmestad, G. G., Jäger, H., Khmelevtsov, S. S., Kolev, I., Kaprieolev, B., Lu, D.-r., Sassen, K., Shamanaev, V. S., Uchino, O., Mizuno, Y., Wandinger, U., Weitkamp, C., Ansmann, A., and Wooldridge, C.: The Experimental Cloud Lidar Pilot Study (ECLIPS)

TCD
8, 4195–4241, 2014

for cloud–radiation research, B. Am. Meteorol. Soc., 75, 1635–1654, doi:10.1175/1520-0477(1994)075<1635:TECLPS>2.0.CO;2, 1994. 4214
Rasmussen, R. M., Vivekanandan, J., Cole, J., Myers, B., and Masters, C.: The estimation of snowfall rate using visibility, J. Appl. Meteorol., 38, 1542–1563, doi:10.1175/1520-0450(1999)038<1542:TEOSRU>2.0.CO;2, 1999. 4213
Rignot, E., Velicogna, I., van den Broeke, M. R., Monaghan, A., and Lenaerts, J. T. M.: Acceleration of the contribution of the Greenland and Antarctic ice sheets to sea level rise, Geophys. Res. Lett., 38, L05503, doi:10.1029/2011GL046583, 2011. 4197
Rusin, N. P.: Meteorological and Radiation Regime of Antarctica (Meteorologicheski i Radiatsionnyi Rezhim Antarktidy), Gidrometeoizdat, Leningrad, 446 pp., 1964. 4200
Schlosser, E., Manning, K. W., Powers, J. G., Duda, M. G., Birnbaum, G., and Fujita, K.: Characteristics of high-precipitation events in Dronning Maud Land, Antarctica, J. Geophys. Res., 115, D14107, doi:10.1029/2009JD013410, 2010. 4219
Shupe, M. D. and Intrieri, J. M.: Cloud radiative forcing of the Arctic surface: the influence of cloud properties, surface albedo, and solar zenith angle, J. Climate, 17, 616–628, doi:10.1175/1520-0442(2004)017<0616:CRFOTA>2.0.CO;2, 2004. 4198
Shupe, M. D., Matrosov, S. Y., and Uttal, T.: Mixed-phase cloud properties derived from surface-based sensors at SHEBA, J. Atmos. Sci., 63, 697–711, doi:10.1175/JAS3659.1, 2006. 4208
Stephens, G. L., Vane, D. G., Boain, R. J., Mace, G. G., Sassen, K., Wang, Z., Illingworth, A. J., O'Connor, E. J., Rossow, W. B., Durden, S. L., Miller, S. D., Austin, R. T., Benedetti, A., Mitrescu, C., and CloudSat Science Team, T.: The CloudSat mission and the a-trains, B. Am. Meteorol. Soc., 83, 1771–1790, doi:10.1175/BAMS-83-12-1771, 2002. 4200
Sun, Z. and Shine, K. P.: Studies of the radiative properties of ice and mixed-phase clouds, Q. J. Roy. Meteorol. Soc., 120, 111–137, doi:10.1002/qj.49712051508, 1994. 4198
Thiery, W., Gorodetskaya, I. V., Bintanja, R., Van Lipzig, N. P. M., Van den Broeke, M. R., Reijmer, C. H., and Kuipers Munneke, P.: Surface and snowdrift sublimation at Princess Elisabeth station, East Antarctica, The Cryosphere, 6, 841–857, doi:10.5194/tc-6-841-2012, 2012. 4198, 4201, 4211, 4217
Thomas, L., Cartwright, J. C., and Wareing, D. P.: Lidar observations of the horizontal orientation of ice crystals in cirrus clouds, Tellus, 42, 211–216, 1990. 4211
Town, M. S., Walden, V. P., and Warren, S. G.: Cloud cover over the South Pole from visual observations, satellite retrievals, and surface-based infrared radiation measurements, J. Climate, 20, 544–559, doi:10.1175/JCLI4005.1, 2007. 4200, 4214

TCD
8, 4195–4241, 2014

Turner, D. D., Vogelmann, A. M., Johnson, K., Miller, M., Austin, R. T., Barnard, J. C., Flynn, C., Long, C., McFarlane, S. A., Cady-Pereira, K., Clough, S. A., Chiu, J. C., Khaiyer, M. M., Liljegren, J., Lin, B., Minnis, P., Marshak, A., Matrosov, S. Y., Min, Q., O'Hirok, W., Wang, Z., and Wiscombe, W.: Thin liquid water clouds: their importance and our challenge, B. Am. Meteorol. Soc., 88, 177–190, doi:10.1175/BAMS-88-2-177, 2007. 4198

Turner, J. and Pendlebury, S. (eds.): The International Antarctic Weather Forecasting Handbook, British Antarctic Survey, Cambridge, UK, available at: http://www.antarctica.ac.uk/met/momu/International_Antarctic_Weather_Forecasting_Handbook/index.php (last access: 23 July 2014), 2004. 4200

Uotila, P., Lynch, A. H., Cassano, J. J., and Cullather, R. I.: Changes in Antarctic net precipitation in the 21st century based on Intergovernmental Panel on Climate Change (IPCC) model scenarios, J. Geophys. Res., 112, D10107, doi:10.1029/2006JD007482, 2007. 4197

Van den Broeke, M., As, D. V., Reijmer, C. H., and de Wal, R. S. V. V.: Surface radiation balance in Antarctica as measured with automatic weather stations, J. Geophys. Res., 109, D09103, doi:10.1029/2003JD004394, 2004. 4215

Van den Broeke, M., Reijmer, C., Van As, D., and Boot, W.: Daily cycle of the surface energy balance in Antarctica and the influence of clouds, Int. J. Climatol., 26, 1587–1605, doi:10.1002/joc.1323, 2006. 4197, 4200

Van den Broeke, M. R., Bamber, J., Lenaerts, J., and Rignot, E.: Ice sheets and sea level: thinking outside the box, Surv. Geophys., 32, 495–505, doi:10.1007/s10712-011-9137-z, 2011. 4197

Van Tricht, K., Gorodetskaya, I. V., Lhermitte, S., Turner, D. D., Schween, J. H., and Van Lipzig, N. P. M.: An improved algorithm for polar cloud-base detection by ceilometer over the ice sheets, Atmos. Meas. Tech., 7, 1153–1167, doi:10.5194/amt-7-1153-2014, 2014. 4203, 4209, 4212, 4213, 4214, 4236

Verlinde, J., Harrington, J. Y., Yannuzzi, V. T., Avramov, A., Greenberg, S., Richardson, S. J., Bahrmann, C. P., McFarquhar, G. M., Zhang, G., Johnson, N., Poellot, M. R., Mather, J. H., Turner, D. D., Eloranta, E. W., Tobin, D. C., Holz, R., Zak, B. D., Ivey, M. D., Prenni, A. J., DeMott, P. J., Daniel, J. S., Kok, G. L., Sassen, K., Spangenberg, D., Minnis, P., Tooman, T. P., Shupe, M., Heymsfield, A. J., and Schofield, R.: The mixed-phase arctic cloud experiment, B. Am. Meteorol. Soc., 88, 205–221, doi:10.1175/BAMS-88-2-205, 2007. 4208

TCD
8, 4195–4241, 2014

Vihma, T., Mattila, O.-P., Pirazzini, R., and Johansson, M. M.: Spatial and temporal variability in summer snow pack in Dronning Maud Land, Antarctica, The Cryosphere, 5, 187–201, doi:10.5194/tc-5-187-2011, 2011. 4197

Wacker, U., Ries, H., and Schättler, U.: Precipitation simulation for Dronning Maud Land using the COSMO Model, Antarct. Sci., 21, 643, doi:10.1017/S0954102009990149, 2009. 4197, 4199

Walden, V. P., Warren, S. G., and Tuttle, E.: Atmospheric ice crystals over the Antarctic plateau in winter, J. Appl. Meteorol., 42, 1391–1405, doi:10.1175/1520-0450(2003)042<1391:AICOTA>2.0.CO;2, 2003. 4205

Walden, V. P., Ellison, M. E., Brandt, R. E., Town, M. S., Hudson, S. R., and Jones, R. M.: Properties of Super-cooled water clouds over South Pole, in: Proc. 8th Conf. Polar Meteorology and Oceanography, San Diego, CA, American Meteorological Society, 2005. 4198

Wang, Z. and Sassen, K.: Cloud type and macrophysical property retrieval using multiple remote sensors, J. Appl. Meteorol., 40, 1665–1682, doi:10.1175/1520-0450(2001)040<1665:CTAMPR>2.0.CO;2, 2001. 4205

Wang, Z., Sassen, K., Whiteman, D. N., and Demoz, B. B.: Studying altocumulus with ice virga using ground-based active and passive remote sensors, J. Appl. Meteorol., 43, 449–460, doi:10.1175/1520-0450(2004)043<0449:SAWIVU>2.0.CO;2, 2004. 4206, 4208

Westbrook, C. D. and Illingworth, A. J.: The formation of ice in a long-lived supercooled layer cloud, Q. J. Roy. Meteorol. Soc., 139, 2209–2221, doi:10.1002/qj.2096, 2013. 4206, 4208

Winker, D. M., Pelon, J., Coakley, J. A., Ackerman, S. A., Charlson, R. J., Colarco, P. R., Flamant, P., Fu, Q., Hoff, R. M., Kittaka, C., Kubar, T. L., Le Treut, H., McCormick, M. P., Mégie, G., Poole, L., Powell, K., Trepte, C., Vaughan, M. A., and Wielicki, B. A.: The CALIPSO mission: a global 3D view of aerosols and clouds, B. Am. Meteorol. Soc., 91, 1211–1229, doi:10.1175/2010BAMS3009.1, 2010. 4200

TCD
8, 4195–4241, 2014

Table 1. Overview of the HYDRANT instruments: raw measured data, derived parameters, location and continuous measurement periods used for analysis (with data gaps < 3 days) until 31 December 2013.

Instrument	Raw data	Derived parameters	Location and measurement period
Ceilometer	Attenuated backscatter vertical profiles ($sr^{-1}\,m^{-1}$)	Cloud base height and vertical extent; cloud phase, optical depth	PE base roof; 1 Feb–30 Mar 2010; 13 Jan–10 Apr 2011; 14 Dec 2011–12 Mar 2012; 1 Jan–16 May 2013; 3–31 Dec 2013.
Infrared radiation pyrometer	Atmospheric brightness temperature (°C)	Equivalent cloud base temperature	PE base roof; 15 Feb–24 Feb 2010; 13 Jan–10 Apr 2011; 1 Jan 2011–12 Mar 2012; 1 Jan–16 May 2013; 8–31 Dec 2013.
Micro Rain Radar	Spectral signal power (mW) per range	Radar reflectivity factor, spectral width, mean Doppler velocity	PE base roof; 18 Jan–31 Mar 2010; 10 Dec 2010–10 Apr 2011; 4 Dec 2011–16 May 2013; 4–31 Dec 2013.
Automatic Weather Station	Near sfc air temperature, RH,pressure,wind speed/dir, SW and LW fluxes, height above snow, snow temperature profile	RH wrt ice, specific humidity, surface albedo, surface temperature, snow accumulation	300 m east of PE base; 2 Feb–21 Nov 2009; 12 Jan–19 Oct 2010; 9 Dec 2010–31 Dec 2013.
Webcam Mobotix M24	Jpeg images at 1 min time res; 70k res.	Weather and instrument monitoring	PE base roof; 29 Jan–10 Apr 2011; 14 Dec 2011–12 Mar 2012; 1 Jan–16 May 2013; 3 Dec–31 Dec 2013.
Snow pit equipment	1 m profile of snow density and temperature, crystal size/shapes	Snow density profile, snow metamorphism	Within 1 km east of AWS; once a year (Dec/Jan)

TCD
8, 4195–4241, 2014

Table 2. Specifications of the HYDRANT ceilometer.

Instrument	Vaisala CL31 ceilometer
Center wavelength	910 ± 10 nm at 25 °C
Operating mode	Pulsed, energy per pulse = 1.2 ± 20 % µJ
Pulse repetition rate	10.0 kHz
Average emitted power	12 mW
Beam divergence	±0.4 mrad edge, ±0.7 mrad diagonal
Field of view divergence	±0.83 mrad
Measurement resolution	10 m (selectable from 10 m or 5 m)
Measurement range	10–7700 m
Reporting interval	15 s (selectable from 2–120 s)
Measurement interval	2 s default (3 s in high-resolution mode)
Environment conditions	−40 to +60 °C, to 100 % RH, up to 50 m s^{-1} wind speed
Minimum recorded beta	10^{-8} sr^{-1} m^{-1}
Protection/shielding	Optical unit is installed inside a white protective shield with automatic lens ventilation (with heating) and internal heating

TCD
8, 4195–4241, 2014

Table 3. Specifications of the HYDRANT infrared pyrometer.

Instrument	Heitronics KT15.82 II Infrared Radiation Pyrometer
Spectral response	8–14 µm
Lens	K6, detector type A, material Ge
Temperature measuring range	−100 to 500 °C
Temperature resolution	0.15 °C at T −25 °C
(emissivitiy 1, response time 1 s)	0.05 °C at T +20 °C
Accuracy (uncertainty)	±0.5 °C + 0.7 % of the difference between target and ambient temperature
Optical field of view (f – 120 mm)	18 mm at 1 mm distance from lens 300 mm at 8 m distance from lens
Sample rate	5 Hz
Operation temperature range	−20 to 60 °C
Protection/shielding	Wooden protective housing with inside temperature at +15 °C and continuous lens ventilation

TCD
8, 4195–4241, 2014

Table 4. Specifications of the HYDRANT Micro Rain Radar.

Instrument	METEK Micro Rain Radar 2 (MRR)
Operating mode	FM-CW Doppler
Spatial coverage	Vertically profiling
Center frequency	24.23 GHz (λ = 1.24 cm)
Frequency modulation	0.5–15 MHz range resolution dependent
Nominal transmit power	50 mW
Antenna dish	Offset parabolic dish, ø = 60 cm
Beam width (2-way, 6 dB)	1.5°
Measurement range	100 m to 3.1 km (at 100 m resolution)
Measurement resolution	100 m (selectable from 30 to 300 m)
Reporting interval	10 s
Environment conditions	Operational at −40 °C to +60 °C; wind speeds up to 45 m s^{-1}
Power consumption	25 W
Installation set up	Natural ventilation of the antenna dish; no antenna heating

TCD
8, 4195–4241, 2014

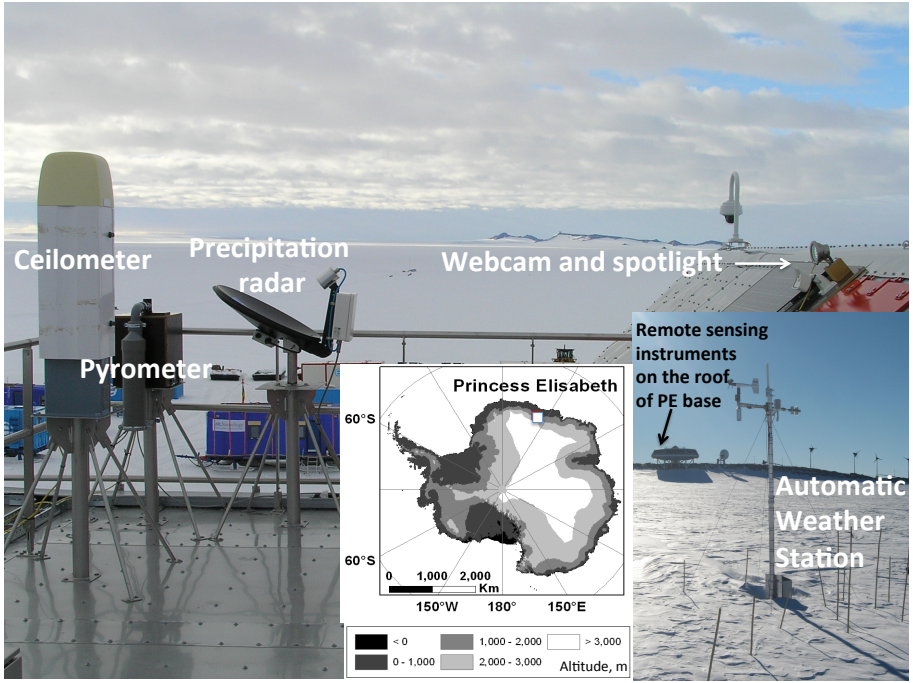

Figure 1. The cloud-precipitation-meteorological observatory HYDRANT at the Princess Elisabeth base in East Antarctica. Shown on the figure are the ceilometer, the infrared pyrometer, the vertically-profiling precipitation radar, the webcam with spotlight and the automatic weather station (right lower inset). The middle inset shows the location of the PE station on the Antarctic ice sheet (white square) together with the orography.

TCD
8, 4195–4241, 2014

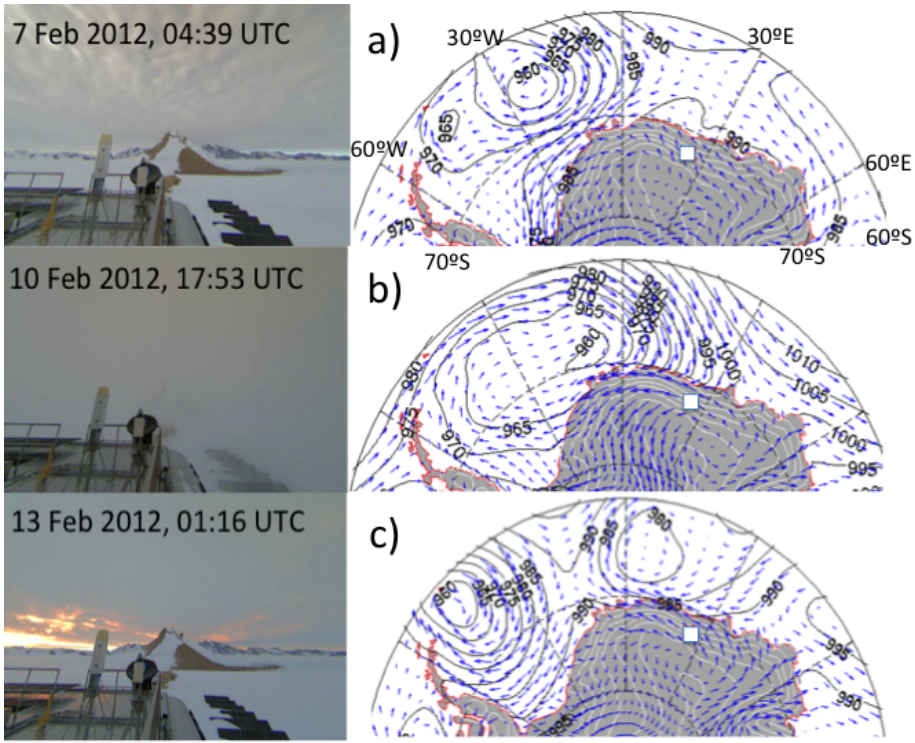

Figure 2. Webcam sky images at specified day and UTC time (left) and maps of corresponding daily mean sea level pressure (contours) and 10 m wind speed (arrows) from ERA-Interim reanalysis data (right) during **(a)** 7 February 2012 (case 1), **(b)** 10 February 2012 (case 2), and **(c)** 13 February 2012 (case 3). The white square indicates the position of PE base. See also webcam movies for each case in the Supplement.

TCD
8, 4195–4241, 2014

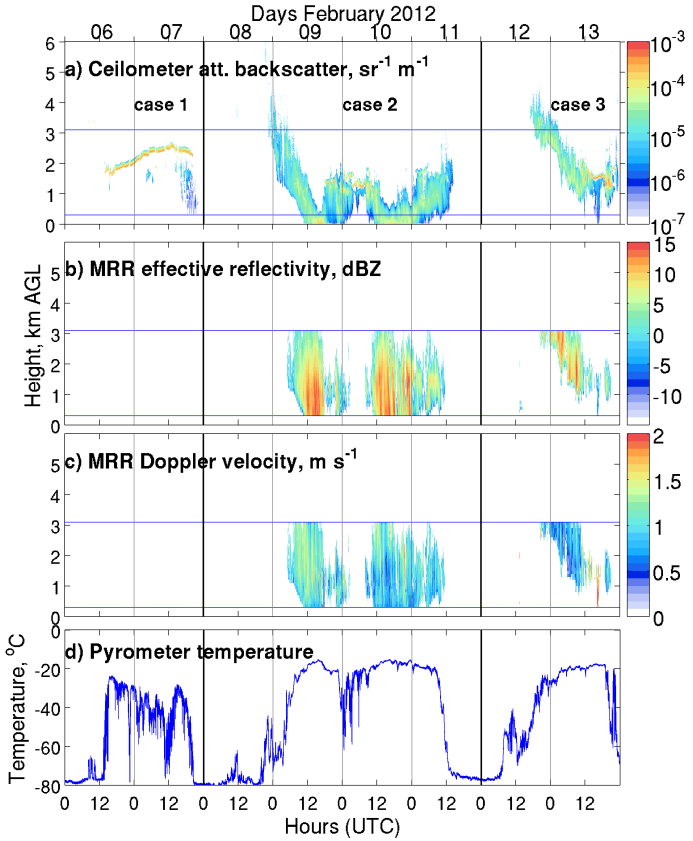

Figure 3. Cloud and precipitation properties derived from ground-based remote sensing instruments during the case period 6–13 February 2012: **(a)** ceilometer attenuated backscatter profiles after the noise-processing and averaging following PT algorithm (Van Tricht et al., 2014), **(b)** MRR radar effective reflectivity profiles, **(c)** MRR mean Doppler velocity profiles, and **(d)** infrared pyrometer temperature.

TCD
8, 4195–4241, 2014

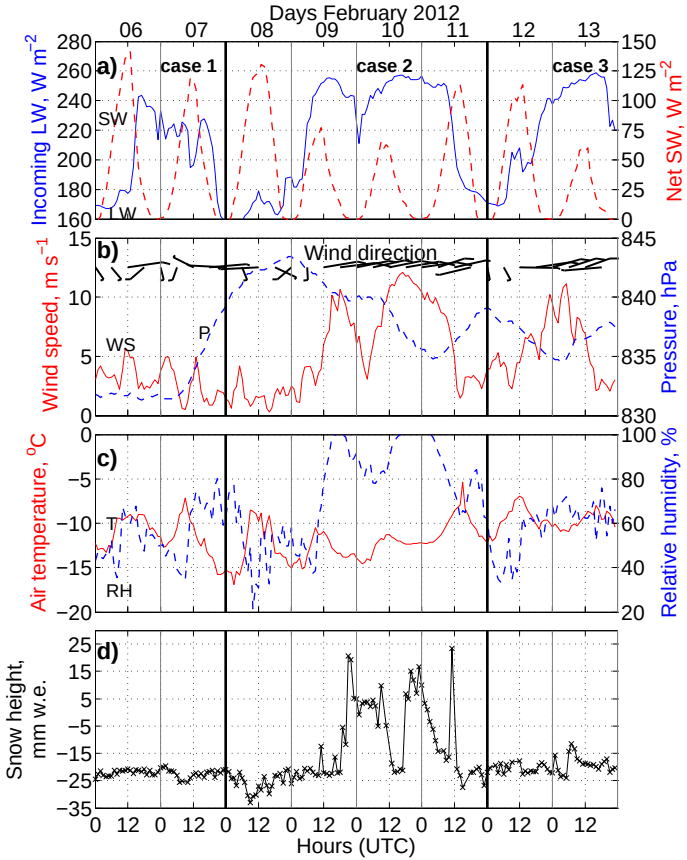

Figure 4. Hourly meteorological parameters during the case period 6–13 February 2012: **(a)** incoming longwave (LW) and net shortwave (SW) fluxes, **(b)** wind speed (WS), wind direction (indicated by "hockey sticks"), and local pressure (P), **(c)** near-surface air temperature (T) and relative humidity with respect to ice (RH), and **(d)** snow height relative to 1 January 2012, 00:00 UTC.

TCD
8, 4195–4241, 2014

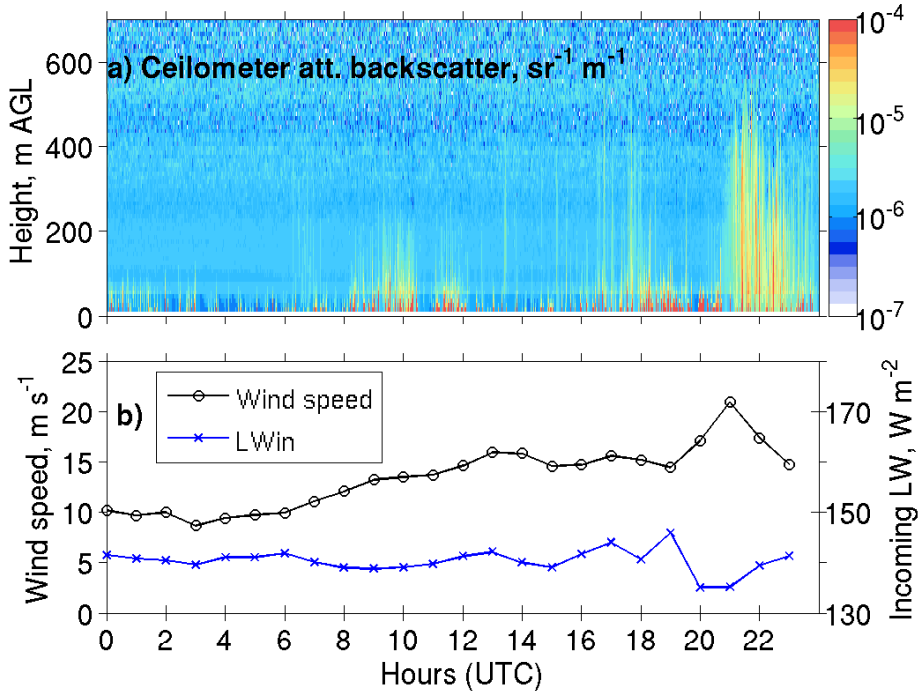

Figure 5. Cloud-free sky blowing snow event on 8 April 2013 (case 4): **(a)** 15 s ceilometer raw attenuated backscatter profiles, and **(b)** hourly mean wind speed and incoming LW flux.

TCD
8, 4195–4241, 2014

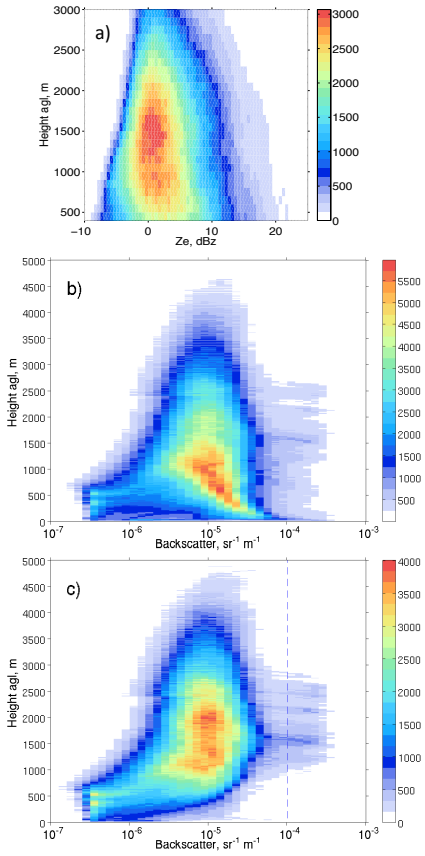

Figure 6. Number of occurrences by height on 1 min temporal scale for **(a)** MRR effective reflectivity (Ze), **(b)** ceilometer backscatter for all cloudy/precipitation profiles, and **(c)** ceilometer backscatter for cloudy profiles excluding snowfall cases (see Sect. 4.2.1). Based on the measurement periods during 2010–2013 indicated in Table 1.

TCD
8, 4195–4241, 2014

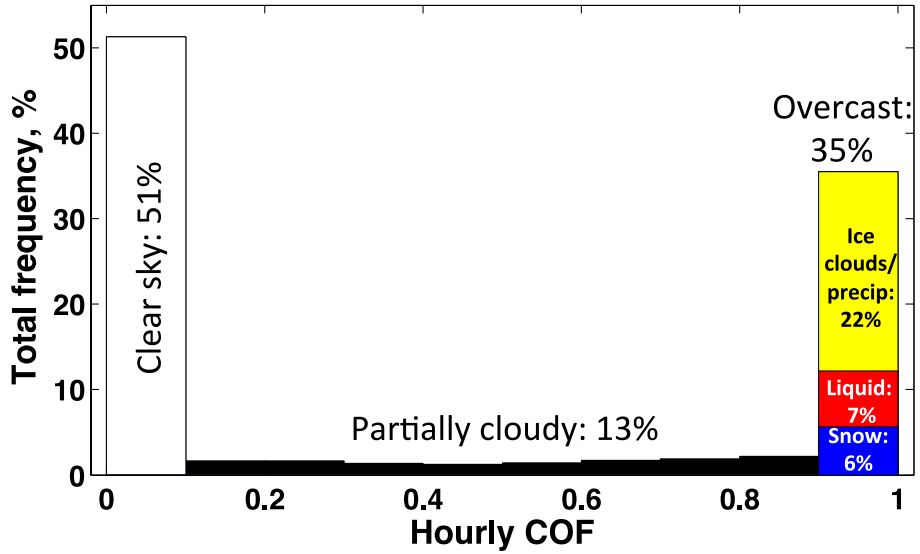

Figure 7. Total frequency relative to the measurement period (%) of hourly mean cloud occurrence frequency (COF, unitless fraction from 0 to 1) for all clouds and precipitation. The column corresponding to COF > 0.9 shows also total frequency of liquid clouds (red), snowfall (blue), and ice clouds/precipitation (including weak snowfalls not detected by MRR) (yellow). Based on the measurement periods during 2010–2013 indicated in Table 1.

TCD
8, 4195–4241, 2014

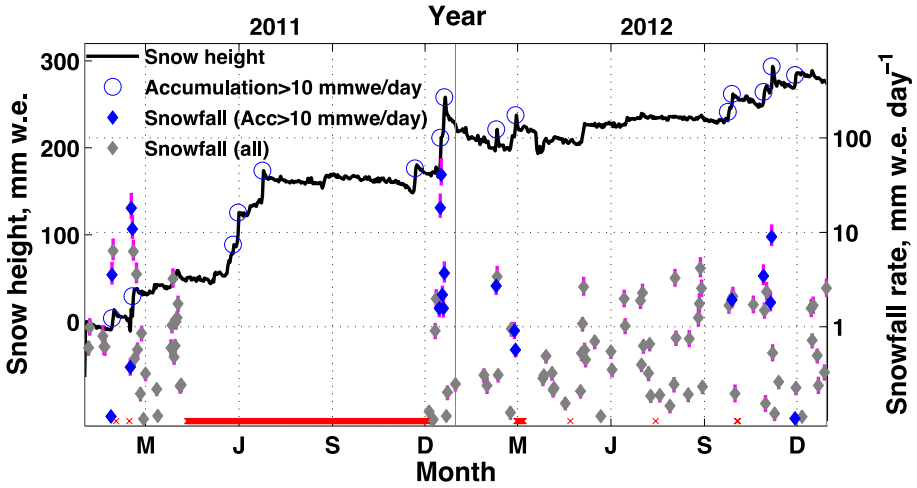

Figure 8. Daily snow height (with respect to 1 January 2011) and snowfall rate (S) during 2011–2012. High accumulation events (> 10 mm w.e. day^{-1}) are marked with blue circles and corresponding snowfall – with blue diamonds. Grey diamonds show all other snowfall events. Vertical magenta lines show uncertainty in S for a range of $Z_e - S$ relationships for dry snow (see Sect. 3.2.3). Horizontal red bar and crosses at bottom indicate gaps in snowfall measurements.

TCD
8, 4195–4241, 2014